Implications of axionic hair on the shadow of M87*

Indrani Banerjee,[*] Subhadip Sau,[†] and Soumitra SenGupta[‡]
School of Physical Sciences, Indian Association for the Cultivation of Science, Kolkata-700032, India

(Received 11 February 2020; accepted 11 May 2020; published 27 May 2020)

The detection of axion fields can unfold intriguing facets of our Universe in several astrophysical and cosmological scenarios. In four dimensions, such a field owes its origin to the completely antisymmetric Kalb-Ramond field strength tensor. Its invisibility in the Solar System–based tests compels one to look for its signatures in the strong-field regime. The recent observation of the shadow of the supermassive black hole in the galaxy M87 ushers in a new opportunity to test for the footprints of axions in the near-horizon regions of black holes, where the gravity is expected to be strong. In this paper, we explore the impact of axions on the black hole shadow and compare the result with the available image of M87*. Our analysis indicates that an axion which violates the energy condition seems to be favored by observations. The implications are discussed.

DOI: 10.1103/PhysRevD.101.104057

I. INTRODUCTION

Axions are pseudoscalar fields which appear as closed string excitations in the heterotic string spectrum [1,2]. In four dimensions, the derivative of such a field is associated with the Hodge dual of the Kalb-Ramond field strength $H_{\alpha\mu\nu}$, which plays a significant role in explaining several astrophysical and cosmological observations. The field strength tensor $H_{\alpha\mu\nu}$ transforms like a third-rank completely antisymmetric tensor field and is associated with a massless second-rank antisymmetric tensor $B_{\mu\nu}$, the so-called Kalb-Ramond field. In higher-dimensional theories, such a field is necessary to unify gravity and electromagnetism [3,4]. Apart from the emergence of such 3-forms in the effective low-energy action of a type-IIB string theory [1,2], they play consequential roles in understanding leptogenesis [5,6], in explaining the cosmic microwave background anisotropy [7,8], and in engendering topological defects which are instrumental in imparting intrinsic angular momentum to galaxies [9,10].

The emergence of superstring theory [1,2] provided a further incentive to investigate the nature and consequences of the Kalb-Ramond field. Its compelling resemblance with spacetime torsion [7,10–18] is noteworthy. In general relativity, the third-rank torsion tensor $T^{\alpha}_{\mu\nu}$ is associated with the antisymmetric part of the affine connection—i.e., $T^{\alpha}_{\mu\nu} = \Gamma^{\alpha}_{\mu\nu} - \Gamma^{\alpha}_{\nu\mu}$—and is primarily antisymmetric in two indices. Its association with the Kalb-Ramond field strength $H_{\alpha\mu\nu}$ becomes evident only when we consider a special subclass of the torsion tensor antisymmetrized in all three indices [11,14–16]. In such a scenario, Einstein gravity with the Kalb-Ramond field in the matter sector is equivalent to a modified theory of gravity incorporating the completely antisymmetric spacetime torsion. Due to this remarkable analogy between spacetime torsion and the Kalb-Ramond field, gravity theories based on twistors necessitate the Kalb-Ramond field [19], and one can show that such a field can successfully generate optical activity in spacetime exhibiting birefringence [20,21].

Moreover, the inefficacy of general relativity in adequately addressing the dark sector [22–25] indicates the need for either some additional matter fields or some alteration in the gravity sector, or both. In such a scenario, inclusion of axions in the matter sector is often considered [26]. Although working with the Kalb-Ramond field or completely antisymmetric spacetime torsion corresponds to the same physical scenario, in this work we will concentrate primarily on modification in the matter sector due to the addition of the Kalb-Ramond field. Given the theoretical significance of such a field, it is instructive to search for the signatures of the Kalb-Ramond field or axions in the available astrophysical and cosmological observations. The attempts to detect the presence of axions in Solar System–based tests—e.g., the bending of light, perihelion precession of Mercury, etc.—reveal that such fields cause minuscule changes compared to general relativity and hence cannot be detected by the present level of precision in the Solar System–based tests [27]. A quest for such a field in the spectrum of quasars has surprisingly revealed that axions which violate the energy condition seem to be favored by astrophysical observations related to black hole accretion [28]. Incidentally, the observed spectrum of the same quasars seems to favor certain classes of alternate gravity theories

[*]tpib@iacs.res.in
[†]tpss2@iacs.res.in
[‡]tpssg@iacs.res.in

—e.g., extra dimensions, Einstein Gauss-Bonnet gravity in higher dimensions, etc. [29–31].

The recent observation of the shadow of the supermassive black hole M87* by the Event Horizon Telescope Collaboration [32–37] has enabled *direct* observations of the near-horizon regime of a black hole. This has opened up a new and independent window to test the nature of strong gravity. The high spatial resolution of the Event Horizon Telescope has facilitated polarimetric imaging of supermassive black holes like M87*, which can be a possible probe to detect the presence of axionic particles [38]. Moreover, based on the findings of the Event Horizon Telescope Collaboration, efforts are being made to establish constraints on the masses of ultralight scalar and vector bosons, which can act as potential dark matter candidates [39].

The aim of this paper is therefore to examine the implications and consequences of axions and the Kalb-Ramond field from the observed shadow of M87*, which will enable us to understand whether the silhouette of M87* favors the presence of such a field.

The paper is broadly classified into five sections. In Sec. II, we study the Einstein field equations with the Kalb-Ramond field as the source and revisit the static, spherically symmetric, and asymptotically flat black hole solution of such equations. Section III is dedicated to investigating the nature of the black hole shadow—first in a general spherically symmetric background in Sec. III A, and subsequently in Sec. III B, where we specialize to the spacetime with axionic hairs presented in Sec. II. In Sec. IV, we investigate the consequences of the Kalb-Ramond field on the recent observation of the shadow of M87*, the supermassive black hole located at the center of the galaxy M87, and finally we conclude with a summary of our findings and implications of our results in Sec. V.

Throughout the paper, the gravitational constant G and the speed of light c are taken to be unity. The metric convention adopted is $(-,+,+,+)$.

II. STATIC SPHERICALLY SYMMETRIC BLACK HOLE SOLUTION IN THE PRESENCE OF THE KALB-RAMOND FIELD

In this section, we discuss the nature of a static, spherically symmetric black hole solution in the presence of the Kalb-Ramond field minimally coupled to gravity [27,40]. The Kalb-Ramond field $B_{\mu\nu}$, which transforms like a second-rank skew-symmetric tensor field, can be considered to be a generalization of the electromagnetic four-potential A_μ [1,11]. The field strength tensor $H_{\alpha\mu\nu}$ associated with the field $B_{\mu\nu}$ consists of a third-rank antisymmetric tensor field and is given by

$$H_{\alpha\mu\nu} = \partial_{[\alpha}B_{\mu\nu]} = \frac{1}{3}[\nabla_\alpha B_{\mu\nu} + \nabla_\mu B_{\nu\alpha} + \nabla_\nu B_{\alpha\mu}] = \frac{1}{3}[\partial_\alpha B_{\mu\nu} + \partial_\mu B_{\nu\alpha} + \partial_\nu B_{\alpha\mu}]. \tag{1}$$

The action associated with the Kalb-Ramond field in four-dimensional Einstein gravity is given by

$$S = \int d^4x\sqrt{-g}\left[\frac{R}{2\kappa^2} - \frac{1}{12}H_{\alpha\mu\nu}H^{\alpha\mu\nu}\right], \tag{2}$$

where g is the determinant of the metric tensor, R is the Ricci scalar, and $\kappa = \sqrt{8\pi G}$ is related to the four-dimensional gravitational constant G. The factor of $-1/12$ has been introduced in the Lagrangian so that one can have the canonical kinetic term as $1/2(\partial_t B_{\mu\nu})^2$ in the local inertial frame. Field equations for the Kalb-Ramond field can be derived by varying the action in Eq. (2) with respect to the field $B_{\mu\nu}$, which yields $\nabla_\mu H^{\mu\nu\rho} = 0$ as the equations of motion. By inspecting the equations of motion, it can be shown that only the spatial components of the field are dynamical. This reduces the propagating degrees of freedom of this field to three, although the Kalb-Ramond field $B_{\mu\nu}$ possesses six independent components in four dimensions. A gauge symmetry $B_{\mu\nu} \to B_{\mu\nu} + \nabla_{[\mu}\chi_{\nu]}$ further reduces the degrees of freedom to zero, as the gauge field χ_μ has three spatial components. However, the gauge field χ_μ exhibits a further invariance $\chi_\mu \to \chi_\mu + \partial_\mu\Phi$, where Φ is a scalar field, and in fact this is the scalar propagating degree of freedom for the Kalb-Ramond field in four dimensions. Additionally, it can be shown that the Kalb-Ramond field satisfies the Bianchi identity given by $\nabla_{[\mu}H_{\alpha\beta\gamma]} = 0$. For a more detailed discussion on the degrees of freedom of the Kalb-Ramond field in arbitrary dimensions, one is referred to Ref. [13]. Since the Kalb-Ramond field has a single propagating degree of freedom in four dimensions, one can express its field strength $H_{\alpha\beta\mu}$ (which is a third-rank antisymmetric tensor field) in terms of the Hodge dual of the derivative of a pseudoscalar field Φ, known as the axion, where

$$H^{\mu\nu\rho} = \epsilon^{\mu\nu\rho\sigma}\partial_\sigma\Phi. \tag{3}$$

Equation (3) enables us to establish the connection between the Kalb-Ramond field and the axion, and throughout the paper, the terms axion and Kalb-Ramond field will be synonymously used.

The variation of the action in Eq. (2) with respect to the metric $g_{\mu\nu}$ leads to the gravitational field equations

$$G_{\mu\nu} = 8\pi G T^{(\mathrm{KR})}_{\mu\nu}, \tag{4}$$

where $G_{\mu\nu}$ is the Einstein tensor and $T^{(\mathrm{KR})}_{\mu\nu}$ is the energy-momentum tensor for the Kalb-Ramond field given by

$$T^{(\mathrm{KR})}_{\mu\nu} = -\frac{2}{\sqrt{-g}}\frac{\delta(\sqrt{-g}\tilde{\mathcal{L}})}{\delta g^{\mu\nu}} = \frac{1}{6}\left[3H_{\mu\rho\sigma}H_\nu{}^{\rho\sigma} - \frac{1}{2}g_{\mu\nu}(H_{\rho\sigma\delta}H^{\rho\sigma\delta})\right], \tag{5}$$

such that $\tilde{\mathcal{L}}$ is the Lagrangian for the Kalb-Ramond field.

Since our goal in this paper is to explore the impact of axions on the shadow of the black hole, we first need to derive the static, spherically symmetric, and asymptotically flat black hole solution of the Einstien's equations given in Eq. (4). This enables us to consider a line element of the form

$$ds^2 = -e^{\nu(r)}dt^2 + e^{\lambda(r)}dr^2 + r^2 d\Omega^2, \tag{6}$$

such that the metric elements $e^{\nu(r)}$ and $e^{\lambda(r)}$ satisfying the Einstein's equations turn out to be two infinite series in $1/r$ [27,40]:

$$e^{\nu(r)} = 1 - \frac{2M}{r} + \frac{bM}{r^3} + \frac{2bM^2}{r^4} + \frac{72bM^3 - 27b^2M}{20r^5} + \cdots, \tag{6a}$$

$$e^{-\lambda(r)} = 1 - \frac{2M}{r} + \frac{3b}{r^2} + \frac{3bM}{r^3} + \frac{4bM^2}{r^4} + \frac{6M^3b}{r^5} - \frac{3b^2M}{4r^5} + \cdots, \tag{6b}$$

where r represents the radial distance from the black hole and b is the axion parameter having units of M^2 (where we have assumed $G = c = 1$). In what follows, we will scale b by M^2 and r by M, such that henceforth we will use the dimensionless parameters b and r throughout this paper. With the Kalb-Ramond field as the source, the above solution has been worked out previously in Refs. [27,40]. For brevity, we do not repeat the derivation here but simply mention the results. From the form of the above metric, it is clear that the presence of the Kalb-Ramond field does not lead to an exact black hole solution but results in perturbations over the Schwarzschild scenario by various powers of the axion parameter b. The solution, however, is valid for all distances, viz., from the event horizon to infinity. This can be confirmed directly from the derivation of the above metric [27]. Since we are considering a spherically symmetric scenario, the axion field Φ depends only on the radial coordinate r. Consequently, from Eq. (3) it is clear that the only nonzero component of the Kalb-Ramond field strength tensor is H^{023}. The energy density corresponding to the Kalb-Ramond field is then given by $H^{023}H_{023} = h(r)^2$. By solving the gravitational field equations and the equations of motion for the Kalb-Ramond field, it can be shown that $h(r)$ assumes the form [27,40]

$$h(r) = \sqrt{\frac{3b}{\kappa}}\frac{1}{r^2}\left[1 + \frac{2}{r} + \frac{4}{r^2} - \left(\frac{8+b}{r^3}\right) + \left(\frac{16+6b}{r^4}\right) + \cdots\right]. \tag{7}$$

From Eq. (7), one can relate that the parameter b in Eqs. (6a) and (6b) is associated with the energy density corresponding to the Kalb-Ramond field or the axion. From Eq. (7), it is clear that at large distances, the Kalb-Ramond field energy density vanishes and we get back to the general relativistic scenario, which is also supported by the form of the solution of the metric [Eqs. (6a) and (6b)]. Therefore, this parametrization of the metric and the Kalb-Ramond field energy density is valid for all distances, although its effect becomes prominent in the near-horizon regime of the black hole.

It is important to note that in order for Eq. (6) to represent a black hole solution, there must be an event horizon. The radius of the horizon r_h is given by solving for $g^{rr} = e^{-\lambda(r)} = 0$, which yields

$$r_h = 1 \pm \sqrt{1 - 3b} \tag{8}$$

if we truncate Eq. (6b) up to the leading-order term in b. The event horizon $r_{\rm eh}$ is given by the positive root of Eq. (8).

In the next section, we will consider the geodesic motion of the photons in the background given by Eq. (6), which will enable us to derive the shape and size of the black hole shadow. It is important to note that the observation of the shadow directly probes the near-horizon regime of black holes where r is small. Therefore, although the leading-order term with the axion appears as a $1/r^3$ correction to the Schwarzschild scenario, its impact on the observed shadow is expected to be significant.

III. GEODESIC MOTION OF PHOTONS AND THE SHADOW OF A BLACK HOLE

The shadow of a black hole refers to the set of directions in the local sky from where electromagnetic radiation just escapes the black hole event horizon and reaches the observer on Earth [41–45]. When light from a distant astrophysical object or the accretion disk surrounding the black hole arrives in the vicinity of the event horizon, a part of it gets trapped inside the horizon, while another part escapes to infinity. This results in a lack of radiation in the observer's sky, leading to a dark patch in the image of the black hole, known as the black hole shadow. The outline of the shadow testifies to the signatures of strong gravitational lensing of nearby radiation, and hence the shape and size of the shadow can reveal valuable information regarding the nature of strong gravity near the black hole [43,46–49]. Consequently, the image of a black hole can be used as a potential probe to estimate the deviation from general relativity.

While the shape of the shadow bears imprints of the background geometry, the size of the shadow scales directly with its mass, reduces with increase in distance, and also exhibits dependence on the background spacetime. For example, a nonspinning black hole always casts a circular shadow [41,42]. In this case, the size of the shadow can be used to investigate the deviation from the

Schwarzschild scenario in general relativity [41,42]. Introducing spin to black holes incurs deviation from the circular shape, and this has been studied extensively in the past, in the context of both general relativity and alternative gravity models [43,46–52]. However, it is important to note that the deviation from circularity becomes apparent only when the angle of inclination of the observer with respect to the rotation axis of the black hole becomes appreciable; i.e., an observer viewing a rotating black hole with zero inclination angle will always see a circular shadow [41,42].

In the next section, we will derive the contour of the black hole shadow in the presence of a general static, spherically symmetric, and asymptotically flat metric given by Eq. (6), and subsequently we will consider the special case with axionic hairs, where the metric components are given by Eqs. (6a) and (6b).

A. Structure of black hole shadow in a general spherically symmetric metric

In this section, we will work out the structure of the black hole shadow in a general static, spherically symmetric background given by Eq. (6). For this purpose, we will study geodesic motion of photons in this spacetime. We consider a geodesic with an affine parameter λ such that the tangent vector is $u^\mu = \dot{x}^\mu = dx^\mu/d\lambda$. The Lagrangian $\mathcal{L}$ corresponding to the motion of test particles assumes the form

$$\mathcal{L}(x^\mu, \dot{x}^\mu) = \frac{1}{2} g_{\mu\nu}\dot{x}^\mu \dot{x}^\nu, \tag{9}$$

such that the action S representing the motion of test particles satisfies the Hamilton-Jacobi equation given by

$$\mathcal{H}(x^\mu, p_\mu) + \frac{\partial S}{\partial \lambda} = 0, \tag{10}$$

where

$$\mathcal{H} = \frac{1}{2} g^{\mu\nu} p_\mu p_\nu = \frac{k}{2} \tag{11}$$

is the Hamiltonian, k is a constant representing the rest mass of the test particles (which is zero for photons), and p_μ is the conjugate momentum corresponding to the coordinate x^μ and is given by

$$p_\mu = \frac{\partial S}{\partial x^\mu} = \frac{\partial \mathcal{L}}{\partial \dot{x}^\mu} = g_{\mu\nu}\dot{x}^\mu. \tag{12}$$

Since the metric does not depend explicitly on t and ϕ, the energy E and the angular momentum L of the photons are conserved. These constants of motion are given by

$$E = -g_{tt}u^t = -p_t \quad \text{and} \tag{12a}$$

$$L = g_{\phi\phi}u^\phi = p_\phi, \tag{12b}$$

respectively. The action S in Eq. (12) can therefore be integrated with the help of Eqs. (12a) and (12b), such that

$$S = -Et + L\phi + \bar{S}(r,\theta), \tag{13}$$

where in the case of a static, spherically symmetrically metric like Eq. (6), $\bar{S}(r,\theta)$ turns out to be separable in r and θ with $\bar{S}(r,\theta) = S^r(r) + S^\theta(\theta)$. We also note that with the help of Eq. (12), Eq. (11) can be written as

$$\begin{aligned} &-e^{-\nu(r)}r^2E^2 + e^{-\lambda(r)}r^2\left(\frac{dS^r}{dr}\right)^2 + L^2 \\ &= -\left(\frac{dS^\theta}{d\theta}\right)^2 - L^2\cot^2(\theta) = -C, \end{aligned} \tag{14}$$

where the separation constant C, known as the Carter constant, represents a third constant of motion [53]. Therefore, the geodesic equations for r and θ are given by

$$\begin{aligned} \left(\frac{dS^r}{dr}\right) &= \sqrt{e^{\lambda(r)}\left(-\frac{C}{r^2} - \frac{L^2}{r^2} + e^{-\nu(r)}E^2\right)} \\ &= E\sqrt{V(r)} = g_{rr}\dot{r} \quad \text{and} \end{aligned} \tag{15}$$

$$\left(\frac{dS^\theta}{d\theta}\right) = \sqrt{C - L^2\cot^2\theta} = E\sqrt{\Theta(\theta)} = g_{\theta\theta}\dot{\theta}, \tag{16}$$

respectively, where

$$V(r) = -\frac{e^{\lambda(r)}\chi}{r^2} - \frac{e^{\lambda(r)}l^2}{r^2} + e^{\lambda(r)-\nu(r)} \tag{17}$$

represents the effective potential in which the photon moves, while

$$\Theta(\theta) = \chi - l^2\cot^2\theta \tag{18}$$

such that $\chi = C/E^2$ and $l = L/E$. The radius of the photon sphere $r_{\rm ph}$ corresponds to the condition where $\dot{r}$ vanishes and the effective potential $V(r)$ has an extremum. This is generally a maximum, which corresponds to an unstable equilibrium of the photon. Given a slight perturbation, the photon either falls into the horizon or escapes to infinity. Due to this reason, the photon sphere plays a crucial role in determining the boundary of the black hole shadow.

Therefore, $r_{\rm ph}$ is obtained by solving $V(r) = V'(r) = 0$, such that the above conditions yield

$$\chi + l^2 = r_{\rm ph}^2 e^{-\nu(r_{\rm ph})} \quad \text{and} \tag{19}$$

$$\chi + l^2 = \frac{1}{2} r_{\rm ph}^3 e^{-\nu(r_{\rm ph})}\nu', \tag{20}$$

respectively. The photon sphere in an arbitrary spherically symmetric metric is therefore obtained by solving for r in the following equation:

$$r_{\rm ph}\nu'(r_{\rm ph}) = 2. \tag{21}$$

In order to derive the contour of the black hole shadow in the observer's sky, one considers the projection of the photon sphere in the image plane [54]. Note that the largest positive radius obtained by solving Eq. (21) is relevant for the computation of the shadow outline [41,42]. The locus of the shadow boundary is denoted in terms of two celestial coordinates α and β, which are related to l and χ [42,54]. This can be understood by expressing the metric in terms of the tetrads, which for a spherically symmetric background assume the form

$$g_{\mu\nu} = e^{(a)}_{\mu} e^{(b)}_{\nu} \eta_{ab}, \quad \text{where} \tag{22}$$

$$e^{(t)}_{\mu} = (e^{\nu/2}, 0, 0, 0), \tag{23a}$$

$$e^{(r)}_{\mu} = (0, e^{\lambda/2}, 0, 0), \tag{23b}$$

$$e^{(\theta)}_{\mu} = (0, 0, r, 0), \tag{23c}$$

$$e^{(\phi)}_{\mu} = (0, 0, 0, r\sin\theta). \tag{23d}$$

Particularly, the apparent velocity $v_{(\theta)}$ of the photon in the θ direction and $v_{(\phi)}$ of the photon in the ϕ direction in the local rest frame are given by

$$v_{(\theta)} = \frac{u_\mu e^{\mu}_{(\theta)}}{u_\mu e^{\mu}_{(t)}} = \frac{p_\theta e^{\theta}_{(\theta)}}{p_t e^{t}_{(t)}} = \frac{\mp\sqrt{\Theta(\theta)}e^{\nu/2}}{r} \quad \text{and} \tag{24}$$

$$v_{(\phi)} = \frac{u_\mu e^{\mu}_{(\phi)}}{u_\mu e^{\mu}_{(t)}} = \frac{p_\phi e^{\phi}_{(\phi)}}{p_t e^{t}_{(t)}} = -\frac{l e^{\nu/2}}{r\sin\theta}, \tag{25}$$

respectively. An observer located at a distance r_0 with an inclination angle θ_0 will perceive that the celestial coordinates are given by

$$\beta = \lim_{r_0\to\infty} r_0 v_{(\theta)}(r_0, \theta_0) = \mp\sqrt{\Theta(\theta_0)}, \tag{26}$$

$$\alpha = \lim_{r_0\to\infty} r_0 v_{(\phi)}(r_0, \theta_0) = -\frac{l}{\sin\theta_0}. \tag{27}$$

Note that r_0 does not appear in the expressions for α and β, since the metric is assumed to be asymptotically flat. Using Eq. (18), it can be shown that

$$\alpha^2 + \beta^2 = \chi + l^2 = r^2_{\rm sh}, \tag{28}$$

which shows that the shadow is circular in shape, where the dependence of its radius $r_{\rm sh}$ on $r_{\rm ph}$ is given by Eq. (19). The above discussion clearly elucidates that for any general static, spherically symmetric, and asymptotically flat metric, the shadow is circular in shape. Further, the radius of the shadow depends only on the g_{tt} component of the metric and is independent of the distance r_0 and the inclination angle θ_0 of the observer.

B. Structure of black hole shadow in the presence of the Kalb-Ramond field

In this section, we will compute the contour of the black hole shadow by considering specifically the spherically symmetric metric with axionic hairs [Eq. (6), with Eqs. (6a) and (6b) as metric elements]. As discussed in the previous section, the radius of the photon sphere is obtained by solving Eq. (21), which for our specific case leads to

$$2r^3 - 6r^2 + 5b = 0. \tag{29}$$

Depending on the value of the axion parameter b, Eq. (29) can have three distinct real roots, one distinct and one coincident real root, or a single distinct real root. The conditions for the above are listed below:

$$\begin{cases} \text{Three distinct real roots}: & 0 < b < 1.6, \\ \text{Only one real root}: & b < 0; b > 1.6, \\ \text{One real and one coincident root}: & b = 0; b = 1.6. \end{cases}$$

The roots of this equation can be obtained analytically by using Cardano's method [55].

When $0 < b < 1.6$, the three real roots are given by

$$r_1 = 1 + 2\cos\left[\frac{1}{3}\cos^{-1}B\right], \tag{30a}$$

$$r_2 = 1 - \cos\left[\frac{1}{3}\cos^{-1}B\right] + \sqrt{3}\sin\left[\frac{1}{3}\cos^{-1}B\right], \tag{30b}$$

$$r_3 = 1 - \cos\left[\frac{1}{3}\cos^{-1}B\right] - \sqrt{3}\sin\left[\frac{1}{3}\cos^{-1}B\right], \tag{30c}$$

with $|B| < 1$, where $B = -1 + 5b/4$. In the event that $b = 0$ or $b = 1.6$, r_2 coincides with r_3, while r_1 corresponds to another distinct real root. When $b < 0$ or $b > 1.6$, which is identical to the situation with $|B| > 1$, there is only one real root, which is given by

$$r_0 = 1 + [\{|B| + \sqrt{B^2 - 1}\}^{1/3} + \{|B| + \sqrt{B^2 - 1}\}^{-1/3}]. \tag{31}$$

The radius of the photon sphere is depicted clearly in Fig. 1(a). In the figure, the blue solid line corresponds to the condition $|B| > 1$, while the red curves constitute the situation with $|B| < 1$. Since the latter consists of three

distinct radii, r_1, r_2, and r_3 are marked with solid, dot-dashed, and dotted red lines, respectively. Among these, the greatest positive root is taken for the computation of the shadow radius. It is important to note that for $b > 1.6$ only one real root exists, but the root is always negative (which is unphysical, since the photon sphere cannot have a negative radius), and hence we conclude that b can never exceed this limit. The maximum value of b is further reduced from the consideration that for the metric to represent a black hole, the event horizon has to be real, which from Eq. (8) implies $b < 1/3 = b_{\rm max}$. Henceforth, we will consider $b_{\rm max}$ to be the upper limit of b.

For the region $b < 0$, Eq. (29) has only one positive real root r_0, which increases as b decreases. It is important to note that b cannot assume arbitrarily large negative values, since when $b \lesssim -1.48 = b_{\rm min}$, the radius of the event horizon $r_{\rm eh}$ exceeds that of the photon sphere $r_{\rm ph}$. Consequently, when b is lower than $b_{\rm min}$, photon circular orbits do not exist. This is an interesting feature the spacetime inherits due to the presence of the Kalb-Ramond background. Therefore, in the remaining discussion we will limit ourselves to the range $-1.48 \lesssim b \lesssim 1/3$. Once the dependence of the photon sphere on b is understood, we compute the radius of the shadow $r_{\rm sh}$ in terms of the axionic parameter b using Eqs. (19) and (28). The variation of $r_{\rm sh}$ with b is plotted in Fig. 1(b), where we have shaded the theoretically allowed region of b. We also note that the shadow expands with negative values of b. This result will have interesting consequences from the observed shadow of M87*, which we discuss in the next section.

We emphasize once again that since we are probing the near-horizon regime, even the leading-order correction to the g_{tt} component of the Schwarzschild metric given by b/r^3 is expected to be significant near the photon sphere. This is in accordance with our analysis, which reveals that the axion parameter plays a crucial role in affecting the radius of the black hole shadow compared to the Schwarzschild scenario [Fig. 1(b)]. Since we are interested in the small-r domain, it might appear that one should also consider the higher-order corrections to the metric (terms over and above the leading-order corrections in the g_{tt} and the g_{rr} components) in Eqs. (6a) and (6b) to study the impact of axions on the black hole shadow and the radius of the event horizon. However, the inclusion of these terms does not significantly affect our results, since b has a theoretical bound of $-1.48 \lesssim b \lesssim 1/3$, and in this domain $b/r < 1$ [Fig. 1(a)], which implies that b/r^3 or b/r^2 are even less. This enables us to truncate the metric in Eqs. (6a) and (6b) up to the leading-order term. However, we verify this approximation explicitly by considering terms up to $1/r^4$ in both g_{tt} and the g_{rr} components of the metric, and we find that this has a negligible effect on our results.

IV. OBSERVED SHADOW OF M87* AND IMPLICATIONS ON AXIONIC HAIR

Using the techniques of VLBI (very large baseline interferometry), the Event Horizon Telescope (EHT) Collaboration has recently released the image of the supermassive black hole M87* at the center of the galaxy M87, thereby opening a new window to test gravity in the strong field regime [32–37]. Their analysis reveals that the angular diameter of the shadow of M87* is $(42 \pm 3)\mu as$, exhibiting a deviation from circularity $\Delta C < 10\%$ and an axis ratio $\Delta A < 4/3$ [32]. This implies that the observed shadow is nearly circular, which is further supported from the fact that the jet axis makes an angle of 17° to the line of sight, which is taken to be the inclination angle of the black hole [32,36,37]. We have already mentioned in Sec. III that noncircular shadows are only possible if a black hole is observed at high inclination angle. This, therefore, justifies our choice of considering the spherically symmetric metric given by Eq. (6), as a first approximation. Hence, the only

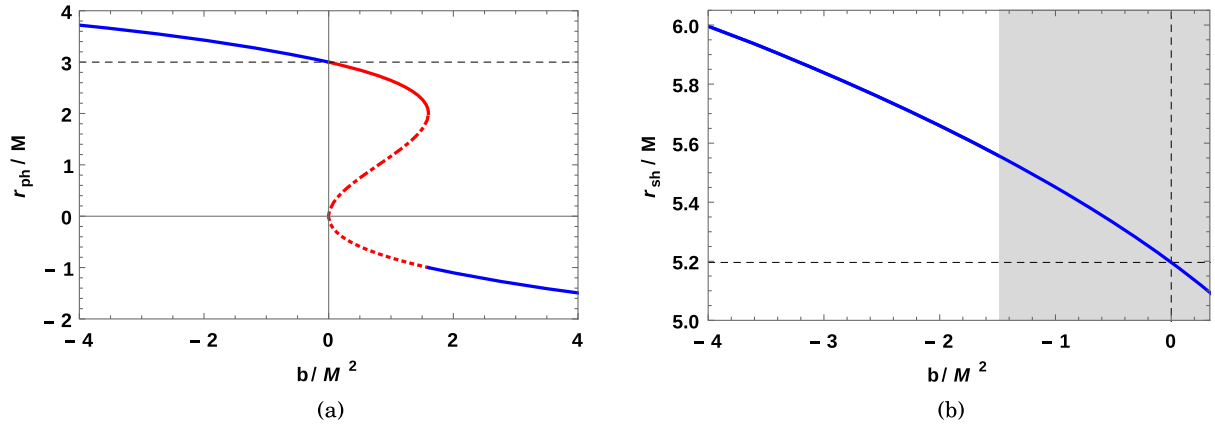

FIG. 1. Dependence of the radius of the photon sphere and the radius of shadow on the axion parameter. (a) Radius of photon sphere vs b. (b) Radius of shadow vs b.

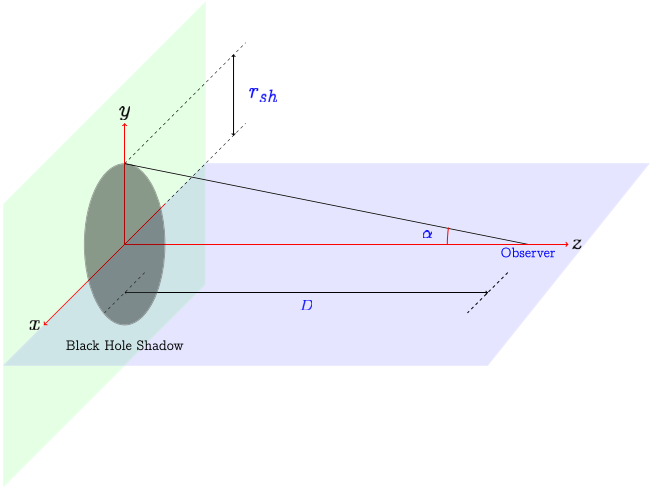

FIG. 2. Black hole shadow with angular diameter 2α.

relevant observable in our context is the angular diameter of the shadow, ΔA and ΔC being trivially equal to one and zero, respectively, satisfying the observed constraint.

The angular diameter of the shadow depends not only on the background metric but also on the mass M of the black hole and its distance D from the observer. This has been illustrated in Fig. 2, which shows that

$$\tan\alpha \approx \alpha = \frac{r_{\rm sh}}{D}, \tag{32}$$

where 2α is the angular diameter. Since the distance between the black hole and the observer is much greater than the radius of the shadow ($r_{\rm sh}$), α is very small, which justifies the approximation in Eq. (32). We have already expressed the radius of the shadow in terms of the metric parameter b in Eq. (6) [e.g., Fig. 1(b)]. Since the radius is in units of GM/c^2, the angular diameter scales directly with the black hole mass. Further, black holes at larger distances will cast smaller shadows.

In the previous section, we have computed the dependence of the axion parameter b on the radius of the photon sphere and the shadow. Therefore, from the magnitude of the observed angular diameter we can comment on the observationally favored values of b. We however require independent measurements of the mass and distance of M87*. Based on stellar dynamics and gas dynamics measurements, the mass of M87* is reported to be $M \sim 6.2^{+1.1}_{-0.5} \times 10^9\ M_\odot$ [56] and $M \sim 3.5^{+0.9}_{-0.3} \times 10^9\ M_\odot$ [57], respectively, while the distance of the source is reported to be $D = (16.8 \pm 0.8)$ Mpc [58–60] from stellar population measurements. Moreover, the mass of the object reported by the EHT Collaboration derived from the angular diameter of the shadow assuming general relativity is $M = (6.5 \pm 0.7) \times 10^9\ M_\odot$ [32,36,37], and hence should not be used to constrain the value of b or other alternate gravity models. Further, the observed emission ring is actually expected to be ∼10% larger than the true shadow size, which is supported by multiple simulations of the accretion flow around M87* [37].

Using these masses and this distance, the theoretical angular diameter of M87* [Eq. (32)] is plotted with b, assuming the mass estimated from gas dynamics observations ($M = 3.5^{+0.9}_{-0.3} \times 10^9\ M_\odot$) in Fig. 3 and from stellar dynamics measurements ($M = 6.2^{+1.1}_{-0.5} \times 10^9\ M_\odot$) in Fig. 4. In Fig. 5, the variation of the angular diameter with b is plotted considering $M = 6.5 \pm 0.7 \times 10^9\ M_\odot$, which is the mass of M87* deduced from the angular diameter of the observed shadow assuming general relativity. Since this is not an independent mass estimation, it should not be used for constraining the value of b from observations related to the shadow, although it can serve the purpose of comparison with the two independent mass measurements. In Figs. 3(a), 4(a), and 5(a), the observed angular diameter of 42 μas is marked with a solid blue line, while the error of ± 3 μas about the centroid value is depicted with blue dashed lines. Figures 3(b), 4(b), and 5(b) are the same as

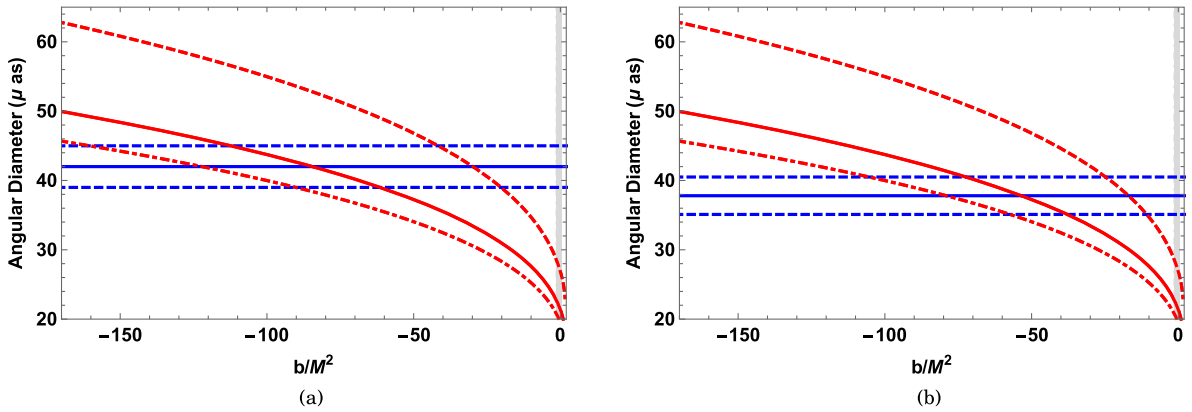

FIG. 3. Variation of the angular diameter of M87* [Eq. (32)] with the axion parameter b, assuming $M = 3.5^{+1.1}_{-0.5} \times 10^9\ M_\odot$ and $D = 16.8$ Mpc. (a) Angular diameter vs b with observed values 42 ± 3 μas marked in blue. (b) Angular diameter vs b with observed values (with 10% offset, 37.8 ± 2.7 μas) marked in blue.

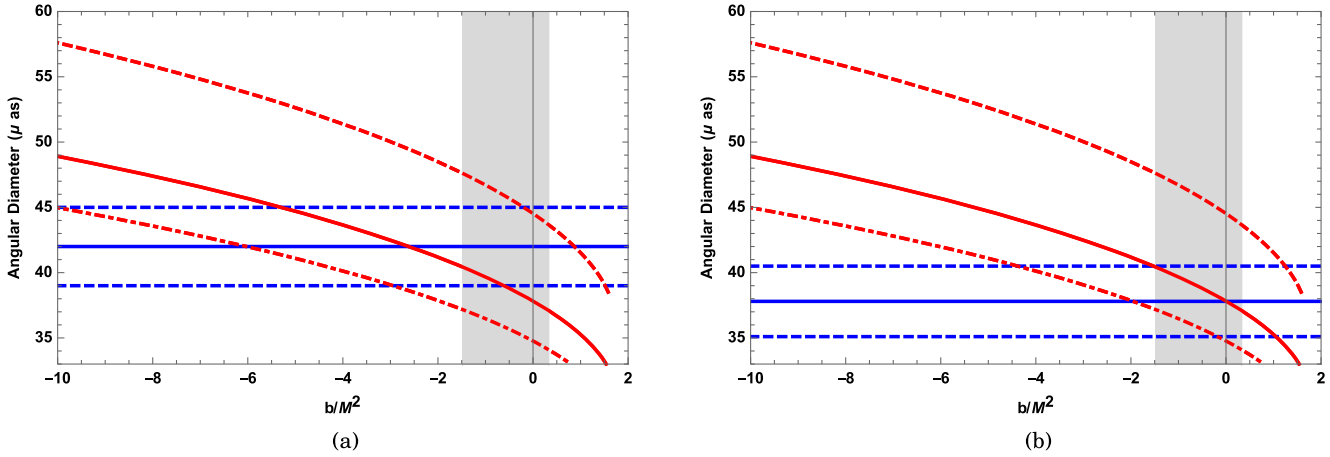

FIG. 4. Variation of the angular diameter of M87* [Eq. (32)] with the axion parameter b, assuming $M = 6.2^{+1.1}_{-0.5} \times 10^9\ M_\odot$ and $D = 16.8$ Mpc. (a) Angular diameter vs b with observed values $42 \pm 3\ \mu$as marked in blue. (b) Angular diameter vs b with observed values (with 10% offset, $37.8 \pm 2.7\ \mu$as) marked in blue.

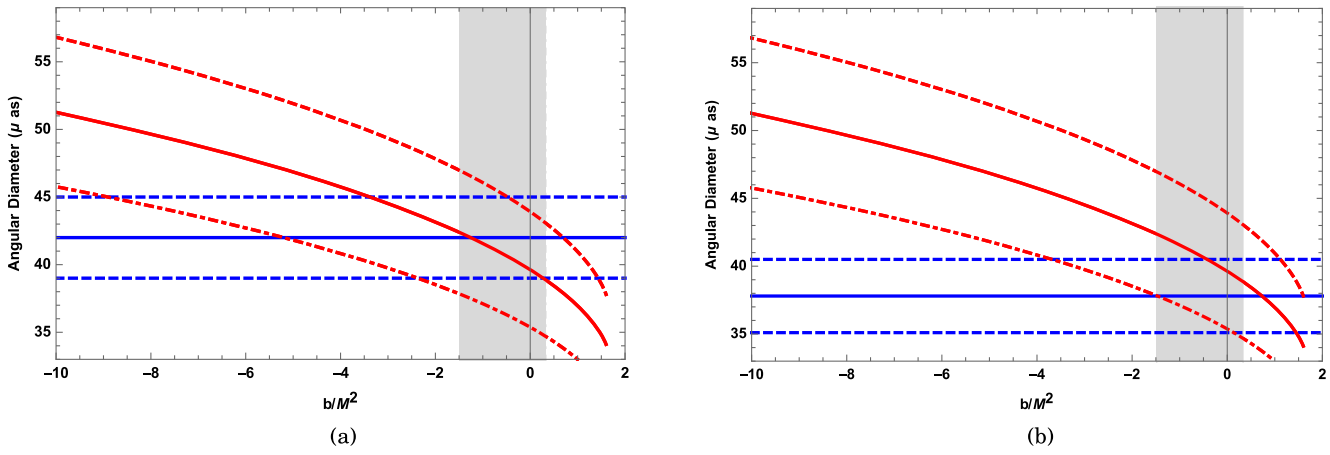

FIG. 5. Variation of the angular diameter of M87* [Eq. (32)] with the axion parameter b, assuming $M = 6.5 \pm 0.7 \times 10^9\ M_\odot$ and $D = 16.8$ Mpc. (a) Angular diameter vs b with observed values $42 \pm 3\ \mu$as marked in blue. (b) Angular diameter vs b with observed values (with 10% offset, $37.8 \pm 2.7\ \mu$as) marked in blue.

Figs. 3(a), 4(a), and 5(a), respectively, except that the observed angular diameter with a 10% offset (i.e., $37.8 \pm 2.7\ \mu$as) is marked with blue lines. In each of the six figures, the theoretical angular diameters are plotted assuming error bars in the masses such that the solid red line corresponds to the centroid value, the dashed red line (above the solid line) is associated with the positive error bar, and the dot-dashed red line (below the solid line) corresponds to the negative error bar in the mass. It is important to note that the angular diameter is inversely proportional to the distance of the source [Eq. (32)], which turns out to be 16.8 ± 0.8 Mpc for M87* (estimated based on stellar population measurements). All the figures (Figs. 3–5) mentioned above are plotted with the centroid value of the distance, i.e., 16.8 Mpc. Also, the theoretically allowed values of b ($-1.48 \lesssim b \lesssim 1/3$) are shaded in all six figures.

Depending on the mass used, the value of b required to explain the observed angular diameter varies. Table I lists the values of b where the observed angular diameter of $42 \pm 3\ \mu$as (Set 1) and $37.8 \pm 2.7\ \mu$as (Set 2) (highlighted in blue in Table I) are reproduced, assuming the three mass estimations of M87* (denoted by Serial Nos. 1, 2, and 3 in Table I). These values of b are essentially obtained at the points of intersection of the blue lines and the red curves in Figs. 3–5.

From Table I, we note that, if $M = 3.5^{+0.9}_{-0.3} \times 10^9\ M_\odot$ is assumed, only negative values of b can explain the observed angular diameter, even when the 10% offset in the angular diameter is considered. This is because the angular diameter scales directly with the mass and the

TABLE I. Values of axion parameter b required to explain the observed angular diameters of 42 ± 3 μas and 37.8 ± 2.7 μas (highlighted in blue). The latter consists of the deviation in the observed angular diameter when a maximum offset of 10% is allowed. The masses used for computing the theoretical angular diameter are reported as Serial Nos. 1, 2 and 3. For $M = 3.5^{+0.9}_{-0.3} \times 10^9\ M_\odot$, the b values are obtained from Fig. 3 when the theoretical angular diameter equals the observed angular diameter of 42 ± 3 μas [Fig. 3(a)] and 37.8 ± 2.7 μas [Fig. 3(b)]. Similarly, for $M = 6.2^{+1.1}_{-0.5} \times 10^9\ M_\odot$, the b values are obtained from Figs. 4(a) and 4(b), while for $M = 6.5 \pm 0.7 \times 10^9\ M_\odot$, the b values correspond to Figs. 5(a) and 5(b).

		Value of parameter b for given values of angular diameter					
		Set 1			Set 2		
Serial No.	Mass (in units of $10^9\ M_\odot$)	45 μas	42 μas	39 μas	40.5 μas	37.8 μas	35.1 μas
1	$3.5 + 0.9$	−42.8	−30.8	−21	−25.2	−17.4	−11.2
	3.5	−115	−86.2	−63	−73	−54	−38.4
	3.5–0.3	−162.4	−124.2	−91.4	−107	−81	−58.8
2	$6.2 + 1.1$	−0.2	0.85	1.47	1.25	1.6	
	6.2	−5.4	−2.65	−0.55	−1.55	0	1.05
	6.2–0.5	−10	−6.2	−2.95	−4.5	−2	−0.25
3	$6.5 + 0.7$	−0.55	0.7	1.4	1.1	1.6	
	6.5	−3.45	−1.3	0.25	−0.45	0.7	1.4
	6.5–0.7	−8.8	−5.3	−2.4	−3.85	−1.45	0.15

shadow radius $r_{\rm sh}$ [Eq. (32)], which increases for a negative b compared to the general relativistic scenario ($b = 0$) [Fig. 1(b)]. Therefore, when a smaller mass of the source is considered, a more negative value of b is required to address the observed angular diameter. For the same reason, when larger masses—i.e., $M = 6.2^{+1.1}_{-0.5} \times 10^9\ M_\odot$ or $M = 6.5 \pm 0.7 \times 10^9\ M_\odot$—are considered, the observationally favored values of b are less negative compared to the case with $M = 3.5^{+0.9}_{-0.3} \times 10^9\ M_\odot$. Further, when the maximum offset of 10% in the angular diameter (i.e., 37.8 ± 2.7 μas) is considered or the positive error bar in the masses are considered, $b = 0$ comes within the error bars. It is evident from Table I and Figs. 4(b) and 5(b) that corresponding to an observed angular diameter of 35.1 μas, no value of b can explain the data when the positive errors associated with masses $M = 6.2 \times 10^9\ M_\odot$ and $M = 6.5 \times 10^9\ M_\odot$ are considered. This is because, with these masses, the value of b required to explain the observed angular diameter of 35.1 μas is $b > 1.6$, which is physically prohibited, since the photon sphere assumes a negative radius beyond this value (Sec. III B). These entries in the table are therefore left blank.

While it is apparent from Table I that a negative b explains the observed angular diameter better, a chi-squared analysis taking into account the uncertainties in the mass, distance, and the accretion flow model is performed to strengthen our conclusion. The chi-squared value is given by

$$\chi^2(b) = \sum_i \frac{\{\mathcal{O} - \mathcal{T}_i(\{M_k\}, \{D_k\}, b)\}^2}{\sigma^2}, \qquad (33)$$

where $\mathcal{O}$ corresponds to the observed angular diameter of 42 μas with a standard deviation $\sigma = \pm 3$ μas, while $\mathcal{T}_i$ represents the theoretical values of the angular diameter depending on the mass M, the distance D, and the axion parameter b. $\mathcal{T}_i$ is evaluated assuming distances between 16.8 ± 0.8 Mpc and masses in the range $M = 6.2^{+1.1}_{-0.5} \times 10^9\ M_\odot$ and $M = 3.5^{+0.9}_{-0.3} \times 10^9\ M_\odot$. The observed emission ring is expected to be 10% larger than the true shadow size if the uncertainties related to the various accretion flow models are considered. Therefore, taking into account the 10% offset, $\mathcal{O} = 37.8 \pm 2.7$ μas also needs to be considered, which is then compared with the model-estimated values $\mathcal{T}_i$.

For a given b, using these allowed values of masses and distances, the χ^2 is computed as in Eq. (33). The variation of χ^2 with the axion parameter b is plotted in Fig. 6, where the red curve corresponds to the situation when $\mathcal{T}_i$ is compared with $\mathcal{O} = 42 \pm 3$ μas, while the magenta curve represents the scenario when $\mathcal{O} = 37.8 \pm 2.7$ μas is used to compute the χ^2. The blue curve is associated with the joint χ^2 when both $\mathcal{O} = 42 \pm 3$ μas and $\mathcal{O} = 37.8 \pm 2.7$ μas are compared with the theoretical values denoted by $\mathcal{T}_i$. All three curves in Fig. 6 illustrate that χ^2 attains the minimum for a negative value of b, where it is important to note that the signature of b is crucial to this work, while its exact magnitude is not so essential to achieve our conclusions. The shaded region in Fig. 6 represents the theoretically allowed range of b, $-1.48 \lesssim b \lesssim 1/3$. In each of the three curves, the χ^2 decreases monotonically as b is reduced from $b_{\rm max} = 1/3$ to $b_{\rm min} = -1.48$, which indicates that within the domain of the allowed values of b, a negative axionic parameter seems to explain the observation better. Such

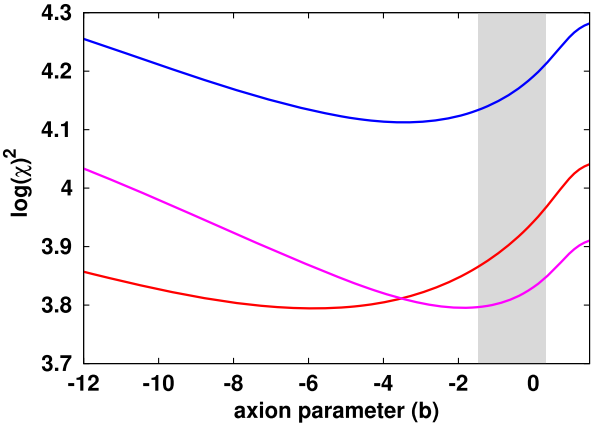

FIG. 6. The figure demonstrates the variation of χ^2 with the axion parameter b obtained by considering the uncertainties in the distances, masses, and the accretion flow models. The red and magenta curves correspond to the situation when $\mathcal{O} = 42 \pm 3$ μas and $\mathcal{O} = 37.8 \pm 2.7$ μas are used for comparison with the theoretical models. The blue curve, on the other hand, represents the scenario when the joint χ^2 is computed taking into account both the aforesaid observations. Interestingly, χ^2 attains the minimum value for a negative b, suggesting that the errors between theoretical estimates of angular diameter and the observations minimize when one considers axions with a negative energy density.

an axion violates the energy condition and has several interesting consequences, which will be disussed in the next section. Interestingly, our present results are in concordance with a previous finding, where we estimated the observationally favored signature of b based on the spectral data of quasars. By comparing the observed spectrum of a set of 80 quasars with the theoretical spectrum from the surrounding accretion disk, we reported that the Kalb-Ramond field violating the energy condition (which is equivalent to a negative axion parameter b) seems to be favored by observations [28]. Since two independent astrophysical observations consistently favor a negative axion parameter, it may be worthwhile to investigate this scenario in the context of other available observations—e.g., quasiperiodic oscillations in the power spectrum of black holes, implications on the signature of b from gravitational wave observations.

V. SUMMARY

In this paper, we aim to investigate the signatures of the Kalb-Ramond field or its dual axion from the recent observations of the shadow of the supermassive black hole in the center of the galaxy M87. This is important, since the weak field tests of gravity lack the necessary precision to discern the presence of such a field while the strong field tests—e.g., the electromagnetic spectrum emitted from the black hole accretion disk—have reported that axion violating the energy condition is observationally favored. Therefore, it is instructive to subject this finding to further tests, and the observation of the black hole shadow provides the appropriate opportunity.

In order to accomplish our goal, we compute the contour of the black hole shadow first in a general spherically symmetric background and note that the radius of the shadow depends only on the g_{tt} component of the metric. Subsequently, we consider the spherically symmetric solution of Einstein's equations solved in the Kalb-Ramond background. Such a metric exhibits a perturbation over the Schwarzschild scenario through the axion parameter b. Since the axion primarily appears as a $1/r^3$ correction to the g_{tt} component of the Schwarzschild metric, its effect on the black hole image which probes the vicinity of the horizon is expected to be significant. Yet we can safely ignore the corrections to the metric with large inverse powers of r due to the theoretical restriction on the axion parameter $-1.48 \lesssim b \lesssim 1/3$, such that in our regime of interest b/r^2 continues to be less than unity. The fact that the magnitude of b is very small from a theoretical consideration is further supported from the observations related to the perihelion precession of Mercury and the bending of light [27]. The theoretical lower bound on negative values of b arises from the absence of any photon circular orbit outside the event horizon. This is an intriguing feature the spacetime exhibits due to the presence of the Kalb-Ramond field.

A stationary, axisymmetric black hole solution of Einstein's equations minimally coupled to the Kalb-Ramond field has not been obtained so far. This, however, does not prevent us from constraining the axion parameter from the shadow of M87*, as the inclination angle of the object is very small, $i \sim 17°$. Consequently, even if M87* is a rapidly rotating black hole, it will cast a circular shadow [41,42,49]. The choice of the spherically symmetric metric is therefore justified. This is further supported by the fact that the observed shadow of M87* has an axis ratio $\Delta A < 4/3$ and a deviation from circularity $\Delta C < 10\%$ [32]. Therefore, the angular diameter, ΔA or ΔC, cannot be used to constrain the spin of M87*. We have verified this explicitly in a previous work [49], where the tidal charge parameter of axisymmetric braneworld black holes could be constrained from the observed angular diameter, but nothing could be concluded about its spin from the observational constraint on ΔC and ΔA. In this context, we would like to mention that there exists the string-inspired Einstein-Maxwell dilaton axion gravity, where the stationary, axisymmetric, and asymptotically flat black hole solution has been worked out and is known as the Kerr-Sen solution in the literature [61,62]. The various fields associated with this theory—namely, the Maxwell field, the axion (or Kalb-Ramond) field, and the dilaton field—depend on r and θ, and the solutions can be found in Ref. [62]. The prospects of constraining such a metric from observations related to the shadow of M87* have been discussed in Ref. [63].

We evaluate the dependence of the shadow radius on the axion parameter b and find that the radius of the shadow decreases with an increase in b, or alternatively, the Schwarzschild metric perturbed with a negative axion parameter casts a larger shadow. It turns out that such an axion or Kalb-Ramond field with a negative energy density bears a greater potential to reproduce the observed angular diameter of M87*, assuming the known distances and masses of the object. We have shown that when the mass estimations of the object based on stellar dynamics ($M = 6.2^{+1.1}_{-0.5} \times 10^9\ M_\odot$) or gas dynamics ($M = 3.5^{+0.9}_{-0.3} \times 10^9\ M_\odot$) observations are considered, and the distance obtained from stellar population measurements (16.8 ± 0.8 Mpc) is used to derive the angular diameter, a negative axion parameter turns out to be a better representation of the data. Only when we consider $M \sim 6.5 \pm 0.7 \times 10^9\ M_\odot$ or allow a 10% offset in the observed image does the $b = 0$ model come within the error bars. One, however, needs to note that the mass of M87* $M \sim 6.5 \pm 0.7 \times 10^9\ M_\odot$ is deduced from the angular diameter of its shadow assuming general relativity, and hence should not be ideally used to constrain the value of b or other alternative gravity models from shadow-related observations. Similarly, the actual shadow size can be at most 10% less than the observed emission ring (due to the uncertainties in the accretion processes), and we show that $b = 0$ becomes viable only when this maximum offset is considered. To support our results, we perform a chi-squared analysis taking into account all the uncertainties in the distances, mass, and accretion models, which explicitly reveals that for a negative axion parameter the χ^2 attains a lower value.

The axion with a negative charge parameter has several interesting astrophysical and cosmological implications. It violates the energy condition, and such a scenario is often invoked for the removal of singularity in geodesic congruences [64], gains ground in bouncing cosmology to prevent the big bang singularity [65], plays a crucial role in altering the Buchdahl's limit for star formation [13], and can potentially generate a nonzero cosmological constant in four dimensions, whose origin is attributed to a bulk Kalb-Ramond field in a higher-dimensional scenario [66]. Moreover, the suppression of the Kalb-Ramond field has been discussed in several physical scenarios—e.g., in the context of warped braneworld models [67] with bulk Kalb-Ramond fields [68,69] and the related stabilization of the modulus [70], in the context of higher-curvature gravity where the associated scalar degrees of freedom diminish the coupling of such a field with the Standard Model fermions [71,72], and in the inflationary era induced by higher-curvature gravity [73,74] and higher dimensions [75].

As a final remark, we mention that in the electromagnetic domain, there is no dearth of spectral data of supermassive black holes, while there is only a single observation of the black hole shadow on which the present result is based. The real challenge of discerning the nature of strong gravity from the black hole spectrum lies in appropriately modeling the spectrum, which depends not only on the background spacetime, but also on the nature of the accretion flow. Disentangling the impact of the metric from the spectrum therefore becomes quite nontrivial. The image of the black hole, on the other hand, provides a much cleaner environment to explore the strong gravity regime. However, in this case, since the angular diameter is highly sensitive to the mass of the black hole, a precise measurement of the black hole mass is necessary to establish strong constraints on the signature of b. This in fact plays a crucial role in constraining b rather than independent observations of horizons with similar levels of uncertainties. In addition to this, the availability of more and more data on black hole images with reduced uncertainties will further enhance the scope to constrain the signature of the axion parameter.

ACKNOWLEDGMENTS

The research of S. S. G. is partially supported by the Science and Engineering Research Board Extramural Research Grant No. (EMR/2017/001372), Government of India. The research of S. S. is funded by CSIR, Government of India.

[1] M. Kalb and P. Ramond, Classical direct interstring action, Phys. Rev. D **9**, 2273 (1974).

[2] M. B. Green, J. H. Schwarz, and E. Witten, *Superstring Theory. Vol. 2: Loop Amplitudes, Anomalies and Phenomenology* (Cambridge University Press, Cambridge, England, 1988).

[3] Y. A. Kubyshin, V. O. Malyshenko, and D. Marn Ricoy, Invariant connections with torsion on group manifolds and their application in Kaluza-Klein theories, J. Math. Phys. (N.Y.) **35**, 310 (1994).

[4] G. German, A. Macias, and O. Obregon, Kaluza-Klein approach in higher dimensional theories of gravity with torsion, Classical Quantum Gravity **10**, 1045 (1993).

[5] N. E. Mavromatos and A. Pilaftsis, Anomalous Majorana neutrino masses from torsionful quantum gravity, Phys. Rev. D **86**, 124038 (2012).

[6] J. Ellis, N. E. Mavromatos, and S. Sarkar, Environmental *CPT* violation in an expanding universe in string theory, Phys. Lett. B **725**, 407 (2013).

[7] A. Lue, L.-M. Wang, and M. Kamionkowski, Cosmological Signature of New Parity Violating Interactions, Phys. Rev. Lett. **83**, 1506 (1999).
[8] D. Maity, P. Majumdar, and S. SenGupta, Parity-violating Kalb-Ramond-Maxwell interactions and CMB anisotropy in a braneworld, J. Cosmol. Astropart. Phys. 04 (2004) 005.
[9] O. Chandia and J. Zanelli, Topological invariants, instantons and chiral anomaly on spaces with torsion, Phys. Rev. D **55**, 7580 (1997).
[10] P. S. Letelier, Spinning strings as torsion line spacetime defects, Classical Quantum Gravity **12**, 471 (1995).
[11] P. Majumdar and S. SenGupta, Parity violating gravitational coupling of electromagnetic fields, Classical Quantum Gravity **16**, L89 (1999).
[12] J. M. Hoff da Silva and R. da Rocha, Torsion effects in braneworld scenarios, Phys. Rev. D **81**, 024021 (2010).
[13] S. Chakraborty and S. SenGupta, Packing extra mass in compact stellar structures: An interplay between Kalb-Ramond field and extra dimensions, J. Cosmol. Astropart. Phys. 05 (2018) 032.
[14] S. Sur and A. S. Bhatia, Weakly dynamic dark energy via metric-scalar couplings with torsion, J. Cosmol. Astropart. Phys. 07 (2017) 039.
[15] F. W. Hehl, P. Von Der Heyde, G. D. Kerlick, and J. M. Nester, General relativity with spin and torsion: Foundations and prospects, Rev. Mod. Phys. **48**, 393 (1976).
[16] V. de Sabbata and C. Sivaram, *Spin and Torsion in Gravitation* (World Scientific, Singapore, 1994), 313 p.
[17] S. Capozziello, G. Lambiase, and C. Stornaiolo, Geometric classification of the torsion tensor in space-time, Ann. Phys. (Berlin) **10**, 713 (2001).
[18] S. SenGupta and A. Sinha, Fermion helicity flip in a Kalb-Ramond background, Phys. Lett. B **514**, 109 (2001).
[19] P. Howe and G. Papadopoulos, Twistor spaces for hyper-Kähler manifolds with torsion, Phys. Lett. B **379**, 80 (1996).
[20] S. Kar, P. Majumdar, S. S. Gupta, and S. Sur, Cosmic optical activity from an inhomogeneous Kalb-Ramond field, Classical Quantum Gravity **19**, 677 (2002).
[21] S. Kar, P. Majumdar, S. SenGupta, and A. Sinha, Does a Kalb-Ramond field make space-time optically active?, Eur. Phys. J. C **23**, 357 (2002).
[22] M. Milgrom, A modification of the Newtonian dynamics: Implications for galaxies, Astrophys. J. **270**, 371 (1983).
[23] T. Clifton, P. G. Ferreira, A. Padilla, and C. Skordis, Modified gravity and cosmology, Phys. Rep. **513**, 1 (2012).
[24] S. Perlmutter *et al.*, Measurements of and from 42 high-redshift supernovae, Astrophys. J. **517**, 565 (1999).
[25] A. G. Riess, A. V. Filippenko, P. Challis, A. Clocchiatti, A. Diercks, P. M. Garnavich, R. L. Gilliland, C. J. Hogan, S. Jha, R. P. Kirshner, B. Leibundgut, M. M. Phillips, D. Reiss, B. P. Schmidt, R. A. Schommer, R. C. Smith, J. Spyromilio, C. Stubbs, N. B. Suntzeff, and J. Tonry, Observational evidence from supernovae for an accelerating universe and a cosmological constant, Astron. J. **116**, 1009 (1998).
[26] A. Dashko and R. Dick, The shadow of dark matter as a shadow of string theory, Eur. Phys. J. C **79**, 312 (2019).
[27] S. Kar, S. SenGupta, and S. Sur, Static spherisymmetric solutions, gravitational lensing and perihelion precession in Einstein-Kalb-Ramond theory, Phys. Rev. D **67**, 044005 (2003).
[28] I. Banerjee, B. Mandal, and S. SenGupta, In quest of axionic hairs in quasars, J. Cosmol. Astropart. Phys. 03 (2018) 039.
[29] I. Banerjee, S. Chakraborty, and S. SenGupta, Excavating black hole continuum spectrum: Possible signatures of scalar hairs and of higher dimensions, Phys. Rev. D **96**, 084035 (2017).
[30] I. Banerjee, S. Chakraborty, and S. SenGupta, Decoding signatures of extra dimensions and estimating spin of quasars from the continuum spectrum, Phys. Rev. D **100**, 044045 (2019).
[31] I. Banerjee, B. Mandal, and S. SenGupta, Does black hole continuum spectrum signal higher curvature gravity in higher dimensions?, Phys. Rev. D **101**, 024013 (2020).
[32] K. Akiyama *et al.* (Event Horizon Telescope Collaboration), First M87 event horizon telescope results. I. The shadow of the supermassive black hole, Astrophys. J. **875**, L1 (2019).
[33] K. Akiyama *et al.* (Event Horizon Telescope Collaboration), First M87 event horizon telescope results. II. Array and instrumentation, Astrophys. J. **875**, L2 (2019).
[34] K. Akiyama *et al.* (Event Horizon Telescope Collaboration), First M87 event horizon telescope results. III. Data processing and calibration, Astrophys. J. **875**, L3 (2019).
[35] K. Akiyama *et al.* (Event Horizon Telescope Collaboration), First M87 event horizon telescope results. IV. Imaging the central supermassive black hole, Astrophys. J. **875**, L4 (2019).
[36] K. Akiyama *et al.* (Event Horizon Telescope Collaboration), First M87 event horizon telescope results. V. Physical origin of the asymmetric ring, Astrophys. J. **875**, L5 (2019).
[37] K. Akiyama *et al.* (Event Horizon Telescope Collaboration), First M87 event horizon telescope results. VI. The shadow and mass of the central black hole, Astrophys. J. **875**, L6 (2019).
[38] Y. Chen, J. Shu, X. Xue, Q. Yuan, and Y. Zhao, Probing Axions with Event Horizon Telescope Polarimetric Measurements, Phys. Rev. Lett. **124**, 061102 (2020).
[39] H. Davoudiasl and P. B. Denton, Ultralight Boson Dark Matter and Event Horizon Telescope Observations of M87*, Phys. Rev. Lett. **123**, 021102 (2019).
[40] S. SenGupta and S. Sur, Spherically symmetric solutions of gravitational field equations in Kalb-Ramond background, Phys. Lett. B **521**, 350 (2001).
[41] P. V. P. Cunha and C. A. R. Herdeiro, Shadows and strong gravitational lensing: A brief review, Gen. Relativ. Gravit. **50**, 42 (2018).
[42] A. de Vries, The apparent shape of a rotating charged black hole, closed photon orbits and the bifurcation set A4, Classical Quantum Gravity **17**, 123 (2000).
[43] S. E. Gralla, D. E. Holz, and R. M. Wald, Black hole shadows, photon rings, and lensing rings, Phys. Rev. D **100**, 024018 (2019).
[44] A. A. Abdujabbarov, L. Rezzolla, and B. J. Ahmedov, A coordinate-independent characterization of a black hole shadow, Mon. Not. R. Astron. Soc. **454**, 2423 (2015).
[45] A. Abdujabbarov, M. Amir, B. Ahmedov, and S. G. Ghosh, Shadow of rotating regular black holes, Phys. Rev. D **93**, 104004 (2016).
[46] C. Bambi, K. Freese, S. Vagnozzi, and L. Visinelli, Testing the rotational nature of the supermassive object M87* from

the circularity and size of its first image, Phys. Rev. D **100**, 044057 (2019).
[47] K. Hioki and K.-I. Maeda, Measurement of the Kerr spin parameter by observation of a compact object's shadow, Phys. Rev. D **80**, 024042 (2009).
[48] S. Vagnozzi and L. Visinelli, Hunting for extra dimensions in the shadow of M87*, Phys. Rev. D **100**, 024020 (2019).
[49] I. Banerjee, S. Chakraborty, and S. SenGupta, Silhouette of M87*: A new window to peek into the world of hidden dimensions, Phys. Rev. D **101**, 041301 (2020).
[50] P. V. P. Cunha, C. A. R. Herdeiro, and M. J. Rodriguez, Does the black hole shadow probe the event horizon geometry?, Phys. Rev. D **97**, 084020 (2018).
[51] Y. Mizuno, Z. Younsi, C. M. Fromm, O. Porth, M. De Laurentis, H. Olivares, H. Falcke, M. Kramer, and L. Rezzolla, The current ability to test theories of gravity with black hole shadows, Nat. Astron. **2**, 585 (2018).
[52] R. Roy and U. A. Yajnik, Evolution of black hole shadow in the presence of ultralight bosons, Phys. Lett. B **803**, 135284 (2020).
[53] B. Carter, Global structure of the Kerr family of gravitational fields, Phys. Rev. **174**, 1559 (1968).
[54] J. M. Bardeen, Timelike and null geodesics in the Kerr metric, in *Black Holes (Les Astres Occlus)*, edited by C. Dewitt and B. S. Dewitt (Gordon and Breach Science Publishers, New York, 1973), pp. 215–240.
[55] R. W. D. Nickalls, Viète, Descartes and the cubic equation, Math. Gaz. **90**, 203 (2006).
[56] K. Gebhardt, J. Adams, D. Richstone, T. R. Lauer, S. M. Faber, K. Gultekin, J. Murphy, and S. Tremaine, The black-hole mass in M87 from Gemini/NIFS adaptive optics observations, Astrophys. J. **729**, 119 (2011).
[57] J. L. Walsh, A. J. Barth, L. C. Ho, and M. Sarzi, The M87 black hole mass from gas-dynamical models of space telescope imaging spectrograph observations, Astrophys. J. **770**, 86 (2013).
[58] J. P. Blakeslee, A. Jordan, S. Mei, P. Cote, L. Ferrarese, L. Infante, E. W. Peng, J. L. Tonry, and M. J. West, The ACS fornax cluster survey. V. Measurement and recalibration of surface brightness fluctuations and a precise value of the Fornax–Virgo relative distance, Astrophys. J. **694**, 556 (2009).
[59] S. Bird, W. E. Harris, J. P. Blakeslee, and C. Flynn, The inner halo of M87: A first direct view of the red-giant population, Astron. Astrophys. **524**, A71 (2010).
[60] M. Cantiello *et al.*, A precise distance to the host galaxy of the binary neutron star merger GW170817 using surface brightness fluctuations, Astrophys. J. **854**, L31 (2018).
[61] A. Sen, Rotating Charged Black Hole Solution in Heterotic String Theory, Phys. Rev. Lett. **69**, 1006 (1992).
[62] C. Ganguly and S. SenGupta, Penrose process in a charged axion-dilaton coupled black hole, Eur. Phys. J. C **76**, 213 (2016).
[63] A. Narang, S. Mohanty, and A. Kumar, Test of Kerr-Sen metric with black hole observations, arXiv:2002.12786.
[64] S. Kar and S. SenGupta, The Raychaudhuri equations: A brief review, Pramana **69**, 49 (2007).
[65] G. De Risi, Bouncing cosmology from Kalb-Ramond braneworld, Phys. Rev. D **77**, 044030 (2008).
[66] S. Chakraborty and S. SenGupta, Solutions on a brane in a bulk spacetime with Kalb-Ramond field, Ann. Phys. (Amsterdam) **367**, 258 (2016).
[67] L. Randall and R. Sundrum, A Large Mass Hierarchy from a Small Extra Dimension, Phys. Rev. Lett. **83**, 3370 (1999).
[68] B. Mukhopadhyaya, S. Sen, and S. SenGupta, Bulk torsion fields in theories with large extra dimensions, Phys. Rev. D **65**, 124021 (2002).
[69] B. Mukhopadhyaya, S. Sen, and S. SenGupta, Does a Randall-Sundrum Scenario Create the Illusion of a Torsion Free Universe?, Phys. Rev. Lett. **89**, 121101 (2002); Erratum, Phys. Rev. Lett. **89**, 259902 (2002).
[70] A. Das, B. Mukhopadhyaya, and S. SenGupta, Why has spacetime torsion such negligible effect on the Universe?, Phys. Rev. D **90**, 107901 (2014).
[71] T. Paul and S. SenGupta, Scalaron tunneling and the fate of antisymmetric tensor fields in $F(R)$ gravity, arXiv:1811.05778.
[72] A. Das, T. Paul, and S. Sengupta, Invisibility of antisymmetric tensor fields in the light of $F(R)$ gravity, Phys. Rev. D **98**, 104002 (2018).
[73] E. Elizalde, S. D. Odintsov, T. Paul, and D. Sez-Chilln Gmez, Inflationary universe in $F(R)$ gravity with antisymmetric tensor fields and their suppression during its evolution, Phys. Rev. D **99**, 063506 (2019).
[74] E. Elizalde, S. D. Odintsov, V. K. Oikonomou, and T. Paul, Logarithmic-corrected R^2 Gravity Inflation in the Presence of Kalb-Ramond Fields, J. Cosmol. Astropart. Phys. 02 (2019) 017.
[75] T. Paul and S. SenGupta, Dynamical suppression of spacetime torsion, Eur. Phys. J. C **79**, 591 (2019).